# New aspects in assessment of changes in width of subarachnoid space with near-infrared transillumination/backscattering sounding, part 1: Monte Carlo numerical modeling

**Jerzy Pluciński**
Gdańsk University of Technology
Department of Optoelectronics
Faculty of Electronics, Telecommunications,
    and Information
ul. Narutowicza 11/12
80-952 Gdańsk, Poland


**Andrzej F. Frydrychowski**
Medical University of Gdańsk
Department of Physiology
ul. Dębinki 1
80-211 Gdańsk, Poland

**Abstract.** A modified Monte Carlo method was used for numerical modeling of the propagation of near-infrared radiation (NIR) within the anatomical layers of the human head. The distribution of NIR transmission between particular anatomical layers in the measurement region (frontal tubers) of the head was obtained. The study demonstrates the effect of the cardiac pump function-dependent changes in the width of the subarachnoid space (SAS) on the intensity of the backscattered radiation. It was proved that the influence of this factor increases with increasing distance between the observation point and the location of the NIR source placed on the surface of the head. Moreover, with sufficiently small NIR detector-source distance, the contribution of the optic radiation propagated within the SAS to the total signal received is negligibly low, which gives a basis for estimation of the modulatory influence of blood circulation within the superficial skin layer on the total intensity of the backscattered radiation. The dimensions of anatomical layers used in the study are real values measured in a female patient, in whom—due to unique circumstances—it was possible to make measurements followed by recordings in clinical conditions, a situation essential for verification of the results of numerical modeling. © 2007 Society of Photo-Optical Instrumentation Engineers. [DOI: 10.1117/1.2757603]

Keywords: transillumination; near-infrared (NIR) radiation; numerical modeling; propagation in tissues of the head; subarachnoid space (SAS).

## 1 Introduction

As a result of long-lasting research focused on noninvasive methods of evaluation of intracranial physiology and pathology that utilize propagation of near-infrared (NIR) radiation, a number of theoretical models of NIR propagation within the tissues of the head were investigated. Several theoretical papers on the modeling of this propagation were published.[1–9] Moreover, two measurement techniques based on these models were developed.

One of the two methods is cerebral oxymetry (NIR spectroscopy), which enables on-line measurement of changes in blood hemoglobin oxygen saturation in superficial cerebral blood vessels. This technique is based on theoretical models devised mainly in Refs. 10–21. The other method is NIR transillumination, which allows for monitoring of the changes in the width of the subarachnoid space (SAS), an important parameter of intracranial homeostasis influenced by a number of significant diseases and disorders (e.g., cerebral edema, brain

tumors, etc.). This method is based on a theoretical model of propagation of optical radiation in the tissues of the human head with particular attention to that in the SAS, which was prepared by one of the authors of this study (Pluciński).[8,9,22]

These models have some common elements, including the propagation of NIR within the scalp, skull bone, and cerebral parenchyma. However, in their models, most of the authors focus more on the determination of optical path length within the brain to calculate the changes in absorption coefficient for oxymetric measurements. Contrary to that, in our model, which was prepared for the transillumination method, we pay particular attention to the propagation of NIR within the SAS—an optical medium of variable width. The knowledge of propagation of the radiation within the SAS at its different and changing dimensions is of key importance for the design of detectors suitable for the transillumination method.

Acquisition of new, unique data from on-line recordings in patients necessitated a revision of the numerical model that we prepared several years ago.[8] On the other hand, the emergence of a new type of equipment—a device capable of recording fast-variable (cardiac-pump dependent or respiration-

Address all correspondence to Jerzy Pluciński, Gdańsk Univ. of Technology, Dept. of Optoelectronics, Faculty of Electronics, Telecommunications, and Information, ul. Narutowicza 11/12, 80–952 Gdańsk, Poland. Tel: +4858 3472642; Fax: +4858 3471848; E-mail: pluc@eti.pg.gda.pl

related) and slow-variable (brain-volume dependent) changes in the SAS width allowed for experimental verification of the numerical model in clinical conditions.

The objective of this study was to verify the theoretical model of propagation of NIR within tissue layers of the head at different SAS widths, utilizing the new, unique data acquired from a special patient who had suffered from traumatic loss of scalp (skin of the head) from one half of the head. Thus, *in vivo* parameters of the head tissues could be determined.

In our study, we decided to explore:

• The relationship and degree of similarity between the power of the signal estimated with numerical modeling and that obtained from live recording from the patient. (This refers to the level of absolute power received by the detector in relation to the source-detector distance, both with and without the superficial skin layer.)

• The importance of the use of two detectors: (a) a distal detector (DD) monitoring the changes of optical signal resulting from fluctuations and oscillations of the width of the SAS (both when the detector is placed on the scalp and directly on the skull bone); (b) a proximal detector (PD) monitoring the changes of signal undergoing retrograde scattering influenced by changes in optical properties of the scalp due to pulsatile flow of blood through the vessels of the skin layer. (The signal from this detector is used for compensation of this influence on the signal detected by the DD.)

• The optimum theoretical positioning of the PD and DD (distance from the source and distance between the detectors), which is important for the transillumination method (enabling monitoring of changes of the width of the SAS).

• The potential appearance of low-order harmonics (second, third, and higher) of the SAS-width-modulated signal, given the fact that transmission of radiation within the SAS in a nonlinear function of the SAS width.

## 2 Numerical Modeling of Transmission of Optical Radiation Within Anatomical Layers of the Head

### 2.1 Description of the Method

Most of the tissues of the head, including skin, skull bone, and brain parenchyma, exert strong scattering effect on the propagating radiation, and this is why modeling of this propagation can be accomplished with good approximation with the method based on diffusion approximation. This approximation, however, cannot be used for low-scattering layers, including the SAS, where most photons cross the layer without a change in the direction of their propagation. Alternative attempts to examine the effect of including a low-scattering region in the head have relied on Monte Carlo models,[4–8,23] finite difference transport models,[24] a hybrid radiosity finite element model,[25,26] or a hybrid radiosity-diffusion model.[3]

In order to achieve the high accuracy of numerical simulation of the propagation of optical radiation within the tissues of the head, the calculations were performed using a dedicated computer program developed by one of authors (Pluciński) and based on a modified Monte Carlo method, briefly outlined here.

The starting point for our consideration is the radiative transport equation (also known as the Boltzmann transport equation) describing the process of light scattering[27]:

$$\frac{1}{v}\frac{\partial L(\mathbf{r},\mathbf{s},t)}{\partial t} = -\mathbf{s}\cdot\nabla L(\mathbf{r},\mathbf{s},t) - \mu_a L(\mathbf{r},\mathbf{s},t) - \mu_s L(\mathbf{r},\mathbf{s},t)$$
$$+ \mu_s\int_{4\pi} p(\mathbf{s},\mathbf{s}')L(\mathbf{r},\mathbf{s}',t)d\Omega + \varepsilon(\mathbf{r},\mathbf{s},t), \quad (1)$$

where $L(\mathbf{r},\mathbf{s},t)$ is the radiance at position $\mathbf{r}$ traveling in a direction $\mathbf{s}$ at time $t$, $p(\mathbf{s},\mathbf{s}')$ is the normalized phase function representing the probability of scattering from the direction $\mathbf{s}$ into a direction $\mathbf{s}'$, $\mu_s$ is the scattering coefficient, $\mu_a$ is the absorption coefficient, $v$ is the speed of optical radiation in the medium ($v=c/n$, $c$ is the speed of optical radiation in vacuum, $n$ is the refractive index of the medium), $\Omega$ is the spatial angle, and $\varepsilon(\mathbf{r},\mathbf{s},t)$ is the power of the source radiation per unit volume per unit solid angle in the directions $\mathbf{s}$ at time $t$.

A Monte Carlo solution of the radiative transport equation involves tracking of simulated photons from collision to collision (for clarity, it should be noted that this use of term "photon" has little in common with the quantum theory of optical radiation but is a simplification used by the Monte Carlo simulation). In collisions, the photons change directions or they are absorbed. We shall not discuss the details of the collisions themselves. The reflections and refractions of light on boundaries between mediums that have different refractive indices are also taken into account. A more efficient algorithm can be obtained if a weight number $w$ is introduced to absorption (and partial reflection) computation.[28,29] As a result, all generated photons can reach the surface of the modeled object and contribute to the modeling result.

The most time consuming computation is that of photon paths between collisions. This is done in a four-step loop until the photon intersects any boundary (between the media having different optical properties) or it is absorbed:

1. For a known photon direction $\mathbf{s}$, a random step size $s_t$ is calculated as $s_t=-\ln(\xi_1)/\mu_s$, where $\mu_s$ is the scattering coefficient and $\xi_1$ is a random number uniformly distributed[29,30] over the interval [0,1]. The new position $\mathbf{r}'$ of the photon is given by $\mathbf{r}'=\mathbf{r}+s_t\mathbf{s}$.

2. A check is made whether the photon crossed a boundary between two mediums having different optical parameters while moving from position $\mathbf{r}$ to position $\mathbf{r}'$. If yes, the position $\mathbf{r}'$ is replaced by a position $\mathbf{r}''$ lying on the boundary, and a new photon direction $\mathbf{s}'$ and new a photon weight $w'$ are calculated using refraction and reflection laws.

3. Absorption is taken into account by calculating a new photon weight $w'=w\exp(-d\mu_a)$, where $w$ is the photon weight in the old position $\mathbf{r}$, $d$ is the distance between the old and the new positions, and $\mu_a$ is the absorption coefficient.[29] If the new photon weight $w'$ is smaller than a prescribed limit $w_{min}$, variance-reducing techniques are used, in particular, "Russian roulette" or "splitting" methods.[31] To reduce the computation time, the calculation of $w'$ can be done only at the moment of the photon exiting the layer ($d$ is then the total distance covered by the photon within the layer up to the moment of exit), while Russian roulette was used when the cumulative distance covered by the photon since its entry to

the layer was greater than a previously calculated distance $d_{max}$, for which $w'$ is smaller than $w_{min}$.

4. Last, we find the new direction of photon propagation $\mathbf{s}'$. The deflection of a photon once it is scattered is specified by the phase function $p(\mathbf{s},\mathbf{s}')$. Since the phase function depends on only one parameter—deflection angle $\theta$ between directions $\mathbf{s}$ and $\mathbf{s}'$—several functions have been discussed in different contexts (isotropic, Henyey-Greenstein, Delta-Eddington, Rayleigh-Gans, etc.) to enable the best fit to experimental data.[32–36] In our simulation, we utilized the Henyey-Greenstein phase function, which describes single scattering in tissue very well. Using this function, the sine and cosine of the angle $\theta$ are obtained from[33]:

$$\cos \theta = \begin{cases} \dfrac{1}{2g}\left[ 1 + g^2 - \left( \dfrac{1-g^2}{1-g+2g\xi_2} \right)^2 \right] & \text{if } g \neq 0, \\ 2\xi_2 - 1 & \text{if } g = 0, \end{cases}$$

$$\sin \theta = (1 - \cos^2 \theta)^{1/2}, \qquad (2)$$

where $\xi_2$ is a random number that is uniformly distributed over the interval $[0,1]$, and $g$ is an anisotropy factor equal to $<\cos \theta>$ and has a value between $-1$ and 1.

The azimuthal angle $\psi$, which is uniformly distributed over the interval 0 to $2\pi$, is given by $\psi = 2\pi\xi_3$, where $\xi_3$ is a random number that is uniformly distributed over the interval $[0,1)$. Having the sine and cosine of the deflection and azimuthal angles, we can find the new direction of photon movement. For this, we have used a modified method of description of photon movement,[37] based on the introduction of a so-called matrix description of the photon direction, allowing for computation time to be reduced compared to the method, which describes direction of photon movement with the use of the vector $\mathbf{s}$.

In this modification, the direction of propagation of a photon is defined with matrix $\mathbf{K}=[\mathbf{k}_x, \mathbf{k}_y, \mathbf{k}_z]^T$ (instead of the vector $\mathbf{s}$), where three orthogonal unit vectors $\mathbf{k}_x =[k_{xx}, k_{xy}, k_{xz}]$, $\mathbf{k}_y=[k_{yx}, k_{yy}, k_{yz}]$, and $\mathbf{k}_z=[k_{zx}, k_{zy}, k_{zz}]$ define a local Cartesian coordinate system whose origin is at the current position of the photon, and $\mathbf{k}_z$ coincides with the direction of the photon propagation. The new direction of propagation is obtained by rotating this system using the Euler rotation theorem. The most common "x convention" is used where the first rotation is by an angle $\psi_E$ about the $z$ axis, the second is by an angle $\theta_E$ about the $x$ axis, and the third is by an angle $\varphi_E$ about the $z$ axis (again). If $\psi_E = \psi - \pi/2$, $\theta_E = \theta$, and $\varphi_E$ is chosen in such a way that $k_{yz}=0$ and the signs of $k_{xz}$ and $k_{zz}$ are opposite, the resulting photon directions are identical to those obtained from Ref. 28. Noticing that the statistical distribution of the sine and cosine of a random angle $\psi$ are equal to those of $\sin(\psi - \pi/2)$ and $\cos(\psi - \pi/2)$, respectively, and that the statistical distribution of the azimuthal angle $\psi$ does not depend on $\varphi_E$, we can set $\psi_E = \psi$, $\theta_E = \theta$, and $\varphi_E = 0$ in Euler formulae, which then become:

$$k'_{xi} = \cos \theta \cos \psi k_{xi} + \cos \theta \sin \psi k_{yi} - \sin \theta k_{zi},$$

$$k'_{yi} = \cos \psi k_{yi} - \sin \psi k_{xi},$$

$$k'_{zi} = \sin \theta \cos \psi k_{xi} + \sin \theta \sin \psi k_{yi} + \cos \theta k_{zi}, \qquad (3)$$

where $i=x$, $y$, or $z$.

In this method, there was one more algorithm modification introduced, designed to enable parallel computations for a number of different widths of the SAS. The modification was that computations of propagation were not repeated for each different width of the SAS for the photons that failed to reach the SAS, accounting for the largest share in the total balance of backscattered radiation. Therefore, it was only for the photons that did reach the SAS that the computations of propagation paths were carried out for each different width of the SAS.

Noteworthy is the fact that in the simulation of photon propagation within the anatomical layers of the head, only a small number of photons reaches the SAS layer. Therefore, in comparison with simulation for just a single SAS width, simulation of photon propagation for multiple SAS widths requires additional computations to be performed exclusively for the quantity of photons reaching the SAS, which is small compared with the total number of photons used for simulation. Moreover, these additional computations related to photon propagation need to be performed for the distance between the SAS and the detector; the assumption is made that the propagation of these photons from the source to the SAS is the same for all the simulated SAS widths. This modification enabled simulations of the fates of a very large number of photons for a number of different SAS widths to be performed on a typical PC, within a reasonable time span. Another advantage of such a modification is that the computed changes of the signal received by the detector, resulting from alterations in the SAS width, are solely due to changes in transmission of these photons that reached the SAS layer. If the simulation were conducted independently for each SAS width, the variance of the computed signal would increase, due to the contribution of the variance of the photons failing to reach the SAS. In other words, for the same number of generated photons, the modified simulation method exhibits a lower variance of the signal incident on the detectors for simulations performed with changing SAS width.

Moreover, in the course of simulations of photon propagation through the anatomical layers of the head, the peak depth reached by each photon prior to its backscattering on the surface of the head was recorded. Based on the knowledge of the peak depth, it can be determined whether a given photon has reached a particular layer. This enabled estimation of not only the total intensity of the radiation backscattered on the surface of the head, but also of the contributions of photons propagated within different tissue layers to the total balance of backscattered radiation. The knowledge of this "breakdown" of the total balance is of particular importance for successful design of the source-detector module for the method of near-infrared transillumination/backscattering sounding (NIR-T/BSS), intended to enable monitoring of the changes in the width of the SAS and capable of compensating the skin-circulation-induced modulation of the optical signal due to pulsatile changes of the optical parameters of the skin of the head.

A key issue in this type of modeling is the accuracy of adopted dimensions of the modeled skull bone with all its sublayers and the skin (scalp), as well as the accuracy of their

**Table 1** Optical parameters of tissues of the head used for numerical modeling.

| Tissue | Thickness (mm) | Absorption Coefficient $\mu_a$ (1/mm) | Reduced Scattering Coefficient $\mu_s'$ (1/mm) | Reference |
|---|---|---|---|---|
| Skin[a,b] | 3 | 0.013 | 1.7 | Ref. 38 |
| Bone—external compact lamina[b,c] | 2 | 0.0242 | 0.88 | Ref. 39 |
| Bone—spongious layer[d] | 5 | 0.01627 | 0.59268 | |
| Bone—internal compact lamina[b,c] | 3 | 0.0242 | 0.88 | |
| SAS[e] | 0 to 5 | 0.001 | 0.001 | |
| Brain[b,f] | 10 | 0.037 | 2.0 | Ref. 40 |

[a]There are major discrepancies between the values of the preceding parameters in works by different authors. This is particularly true in the case of the absorption coefficient [e.g., its value can be $\mu_a = 0.013$ 1/mm (Ref. 38), or even $\mu_a = 0.27$ 1/mm (Ref. 41) or $\mu_a = 0.45$ 1/mm (Ref. 42)]. Our earlier experience indicates, however, that the two latter values are highly exaggerated for individuals of Caucasian origin. It seems that the real values are best approximated by the parameters reported by Simpsony.[38] Optical parameters of the skin provided by Simpsony were also used by Okada in his works on NIR propagation within tissues of the head, e.g., Refs. 4–6. Therefore, we also decided to apply those parameters reported in Ref. 38 in our model.
[b]At distances from the source markedly exceeding $1/\mu_s$, power distribution does not depend on the scattering coefficient and scattering anisotropy coefficient, if the reduced scattering coefficient $\mu_s'[\mu_s' = \mu_s(1-g)]$ remains constant. Therefore, in order to reduce the computation time, an isotropic model of propagation of radiation within the skin, bones, SAS, and brain was assumed in which $g=0$ and $\mu_s = \mu_s'$.
[c]In Ref. 39, parameters for the skull were given for 849 nm and 956 nm wavelengths. The value for 870 nm, needed for our calculations, was obtained through linear approximation.
[d]Inthe analyzed case, the measured density of the spongious bone layer was 3.29 times less than that of the compact bone lamina.
[e]The width of the fluid layer in the SAS was changed in the range from 0 to 5 mm; calculations were made with increment 0.1 mm. Absorption and scatter were neglected because they are minute compared with the bordering tissues; however, nonzero values for both absorption and scatter coefficients were assigned (0.001 l/mm and 0.001 l/mm, respectively) in order to avoid division by zero in the calculation procedure. The scatter anisotropy coefficient was assumed to be of 0 value.
[f]The width of the fluid layer was assumed to be much greater than in real conditions (about 4 mm) and much greater than the depth of the intracerebral penetration by NIR. The depth of penetration is equal to $(1/\{3\mu_a[\mu_a + (1-g)\mu_s]\})$ (Ref. 43), which is much less than the width of the brain. (For a brain width of $\mu_a = 0.037$ 1/mm, $\mu_s' = 2.0$ 1/mm, at 870 nm, the depth of brain tissue penetration equals 2.1 mm.) Such an assumption eliminates the need for modeling the deeper layers of the brain in this model study. Increasing the depth of penetration in this model study led to a marked increase in model calculation time, with no change observed in the distribution of the power of radiation on the surface of the head. In studies by other authors, other values of parameters for brain parenchyma can also be found, e.g., in Ref. 44, $\mu_a = 0.03$ 1/mm and $\mu_s' = 1.56$ 1/mm at 870 nm.

optical parameters. The results of simulation of propagation of NIR optical radiation within the tissues of the head as well as the results of *in vivo* recordings presented later refer to a unique medical case of unilateral loss of the skin layer of the head as a result of injury.

On the side with scalp removed, skull bone was excised to enable coverage of the missing surface with transplanted skin. Thus, measurements were possible on the excised fragment of the frontal bone (usual site of detector placement), determining both the width of the component bone layers (internal compact layer, spongious layer, and external compact layer) and their density.

The measured width of the skin of the head was approximately 3 mm. The widths of the internal and external compact layers of the bone were measured in the excised fragment of the frontal bone. The ratio of specific gravities of both these layers was also calculated. This ratio enabled estimation of the scattering and absorption coefficients for the spongious layer on the basis of the values of these coefficients for the compact bone, with the assumption that the contribution of scattering and absorption within the pores of the bone is negligible, compared to that in the compact bone constituting the bone trabecules. These pores, however, contribute to an increase in the mean distance between the scattering or absorption centers. As the trabecules within the spongious bone are made of the same material as the compact bone, it should be noted that with an *n*-times increase of the distances, at a given mass of the bone tissue, the spatial dimensions of the bone would have to increase *n* times as well, on the assumption that the mass of air within the pores is neglectably low compared to that of the bone material, and the volume of the bone would have to increase $n^3$-times. Thus, density of the bone would be reduced $n^3$-times, too. For this reason, we assumed that the scattering and absorption coefficients are proportional to the third root of the ratio of specific gravities of both these layers. Other material constants were taken from reference data provided in reports by other authors. Dimensions of specific anatomical layers of the head along with their optical parameters used for simulations are provided in Table 1. These param-
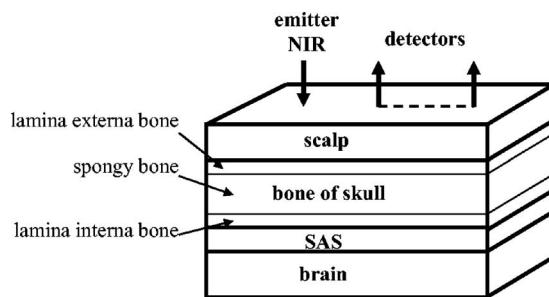
**Fig. 1** Simplified diagram presentation of a vertical section of a block of tissues of the head, with NIR conducting layers identified.



**Fig. 2** NIR-BSR power density on the surface of the head with scalp intact as a function of source-detector distance and SAS width, for source power 1 W.

eters are valid for a wavelength of 870 nm, which was applied in the measurements in the patients—see part 2 of this study.[45]

Schematic presentation of particular anatomical layers of the head is presented in Fig. 1. For the sake of simplification, in the model it was assumed that the particular anatomical layers (except the SAS) constitute zones of one, fixed width (Fig. 1). Fresnel reflection, resulting from the refractive index difference, was taken into account, but only at the skin-air border (a skin refractive index of 1.35 was assumed). In the model, it was also assumed that the NIR source is a light-emitting diode (LED; power $P = 1$ W, wavelength $\lambda = 870$ nm, and 2.5-mm diam) generating a divergent beam of divergence angle $\approx 60$ deg. (The diameter and divergence angle of the model NIR source were equal to those of the actual LED used in real *in vivo* measurements in the patient.) In the process of modeling, photons of backscattered NIR radiation (NIR-BSR) were recorded.

Modeling was performed for 100 million photons generated by the source. This number is the result of a compromise between the accuracy of simulation (low variance of the output data) and the computation time—a typical PC machine (Athlon 64 3000+) was used and total model computation time for the SAS range 0 to 5 mm with step 0.1 mm was 36 h 22 min for all tissue layers (scalp included) and 36 h 17 min for the scalp-free tissue set.

As will be demonstrated in part 2 of this study,[45] the number of photons used for simulation resulted in negligibly low variance of the output data, proved by the lack of fluctuations in most of the examples of a change in source-detector separation or a change in the SAS width. It was only at the longest source-detector distance, when the detector is reached by a relatively low number of photons, that minor fluctuations can be noticed, which proves that the number of photons selected for simulation guarantees high precision of simulation at the adopted parameters of particular layers. When needed, the variance of the received output data can be easily determined based on these fluctuations.

### 2.2 Results of Numerical Simulations

### 2.2.1 Results of modeling of NIR propagation within tissues of the head: scalp included

For the estimation of the NIR-BSR power, received by a detector placed on the surface of the head, density of that radiation was calculated in the function of both the source-detector distance and the SAS width (Fig. 2). The presented results of
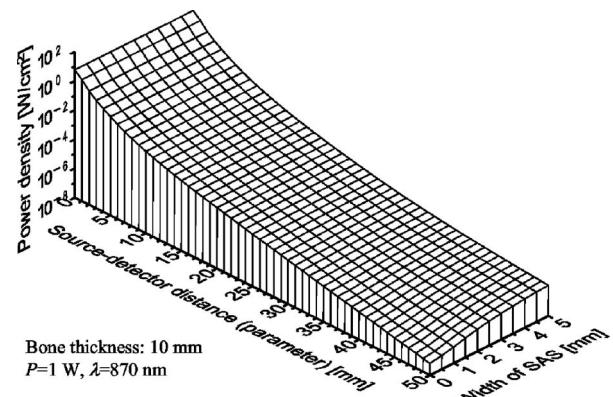
modeling of NIR-BSR density were obtained assuming a source of 1 W power. NIR-BSR power density for a light source of the power $P_{source}$ other than 1 W can be obtained by multiplication of the received power density by the power ratio $P_{source}/1$ W. Power level of the signal received by a particular photodiode can be obtained by multiplying the active area of the detector by NIR-BSR power density for the power of the source applied.

For the purpose of noninvasive assessment of changes in the SAS width with NIR, it is essential to obtain information on the changes in NIR-BSR power density in the function of the SAS width, rather than on the absolute power level of NIR-BSR received. To achieve this, it is very useful to calculate power density on the surface of the head, normalized against the maximum power received by the detector at a given source-detector distance. This normalized power density is presented in Fig. 3. The simulation clearly shows that the depth of modulation of the signal received by the detector resulting from the changes in the SAS width increases with the increase of source-detector distance. The obtained relationships also indicate that the function describing dependence of the signal power on the SAS width is nonlinear. The nonlinearity is particularly prominent for source-detector dis-
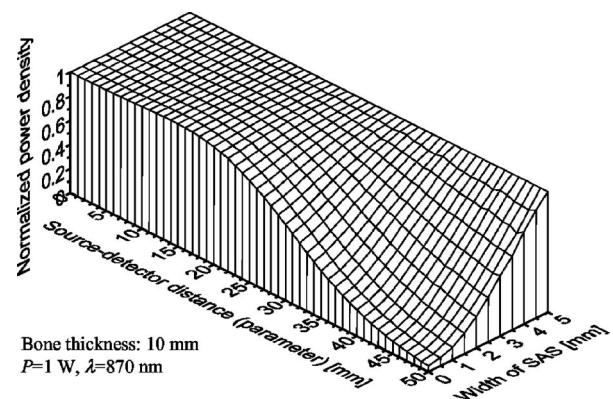


**Fig. 3** Relative changes in received power density of NIR-BSR versus the width of the SAS for a given source-detector distance for head with scalp intact.
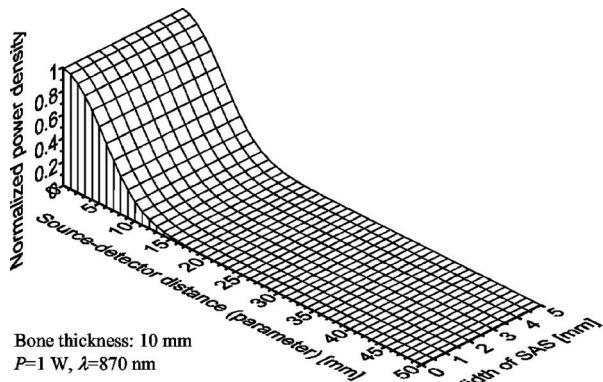
**Fig. 4** Contribution of radiation propagated within the skin only to the total NIR-BSR received by the detector as a function of the source-detector distance and SAS width for part of the head with scalp intact.



**Fig. 6** Contribution of radiation propagated within the SAS to the total NIR-BSR received by the detector as a function of source-detector distance and SAS width for head tissues with scalp included.

tance exceeding 30 mm, especially at SAS width below 2 mm. This nonlinearity must be taken into account in frequency analysis of the received signal, which is one of the techniques of assessment of cerebral edema. In the initial phase of this pathology, the SAS width is decreased and, depending on the degree of edema, may transiently approach zero value at the peak of the systolic phase of the cardiac cycle. In such circumstances, a greater relative contribution of the harmonics to the total energy within the signal frequency spectrum can be expected. Yet with a nonlinear relationship between radiation intensity and the SAS width, at sinusoidal pattern of changes of that width under the influence of the cyclic function of the heart—as expected with sinusoidal changes of cerebrospinal fluid pressure[46,47]—harmonics may also appear, which can make detection of the initial phase of cerebral edema on the basis of measurement interpretation more difficult than if the relationship were linear.

It is important to notice that modulation of optical parameters of the tissues, e.g., under the influence of changes of blood content within the tissues with pulsatile blood flow, could result in the modulation of the signal received by the detector. Such modulation is possible mainly in the scalp. The influence of skin-blood-flow-related modulation on the signal
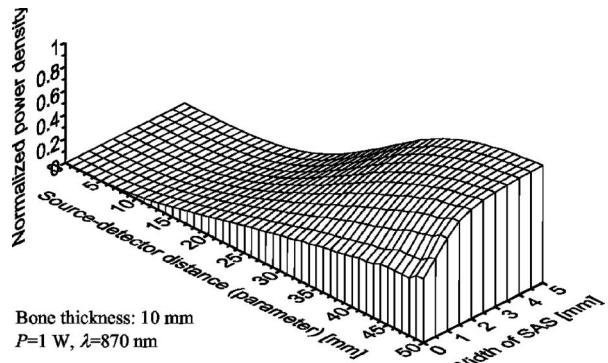
can be eliminated by using two detectors: the PD located close enough to the light source to record radiation propagated from the source through the skin or skin and bone only; and the DD located farther from the source and receiving radiation propagated mostly within the SAS. To enable selection of appropriate source-detector distances for both detectors, shares in the total NIR-BSR balance were calculated for radiation propagated within the scalp only, within the scalp and bone only, and within the SAS. These contributions are presented in sequence in Figs. 4–6. The relationships presented in these figures show that as the source-detector distance increases, the contribution of the radiation propagated within the skin or skin and skull bone only decreases, while that of radiation propagated within the SAS increases.

Further analysis, whose results are presented in Figs. 7 and 8, yields the contribution of transmission within particular tissue layers of the head to the total NIR-BSR. This analysis enables us to determine the optimum positioning of the PD and DD. The PD should be located far enough from the NIR source to ensure that the signal it receives is based mostly on NIR transmission within the skin and bone rather than on the transmission within the skin only. With such a setting, it is guaranteed that the optical signal crosses the skin (scalp) twice: from the surface of the head on its way to the deeper
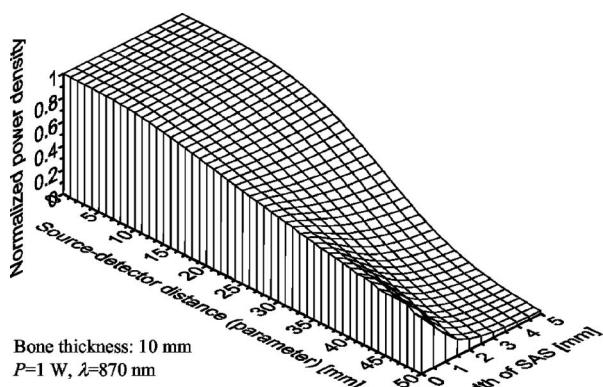


**Fig. 5** Contribution of radiation propagated within the skin and bone only to the total NIR-BSR received by the detector as a function of source-detector distance and SAS width for the part of the head with scalp intact.
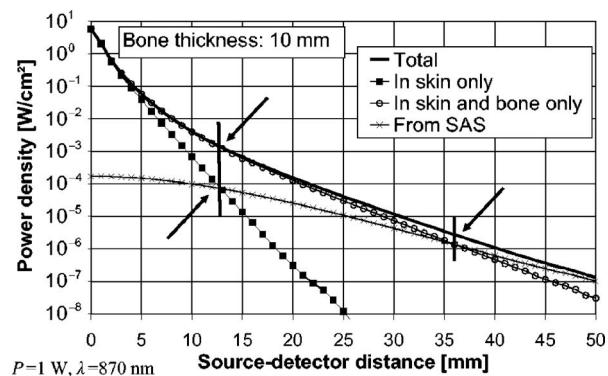


**Fig. 7** Power density of NIR-BSR on the surface of the head and the contribution of radiation: transmitted within the skin only, transmitted in the skin and skull bone only, and propagated within the SAS, for SAS width 1 mm and source power of 1 W, for tissues of the head including the scalp.
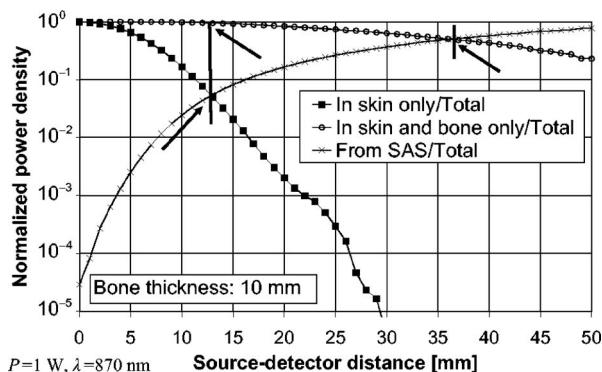
**Fig. 8** Relative contribution of radiation: transmitted in the skin only, transmitted in the skin and skull bone only, and propagated within the SAS, for head with scalp intact, in the total balance of NIR-BSR.



**Fig. 9** NIR-BSR power density on the surface of the scalp-void head as a function of source-detector distance and SAS width, for source power 1 W.

anatomical layers of the head, and again on the return from the deeper layers toward the detector. Noteworthy, the signal received after transmission in the SAS has the same history of twice crossing the scalp layer. With the detector positioned too close to the source, the detector would also record the signal transmitted longitudinally within the scalp layer, parallel to other layers and skin surface. Such a signal would be much more difficult to use for compensation of the signal modulation resulting from changes of optical parameters of the scalp due to pulsatile blood flow within this layer.

If we assume that the signal resulting from transmission of radiation within the anatomical layers of the head deeper than skin should be at least 10 times greater than that propagated within the skin only, then the source-PD distance should be greater than 11.5 mm.

On the other hand, PD distance from the source should not exceed the maximum distance for which the contribution in total NIR-BSR of the radiation propagated within the skin only is still greater than that of the radiation propagated within the SAS. The performed simulation indicates that source-PD distance should not exceed about 13 mm. This distance is marked on Figs. 7 and 8 with thick vertical lines in the left parts of the charts. The lower arrow at that line indicates the source-PD distance value at which the intensity of the backscattered radiation transmitted within the skin balances only that of radiation propagated within the SAS. The upper arrow at that line shows the contribution of the radiation propagated only within the scalp and skull bone collectively. It would be better if the PD receives much more radiation propagated within the skin only than of that transmitted within the SAS. Assuming that the ratio of the two should be greater than 10, the source-PD distance should be lower than $\approx 9.5$ mm.

Based on the preceding analysis, it appears impossible to find such a PD position at which simultaneously contribution of transmission within anatomical layers deeper than the scalp would be 10 times greater than of that within the scalp only and contribution of transmission within the scalp only would be 10 times greater than of that within the SAS. Anticipating strong modulation of radiation propagated within the SAS, caused by pulsatile changes in the width of that space, it seems appropriate and fully justified to strongly adhere to the second condition, with a softer approach to the first one. If we
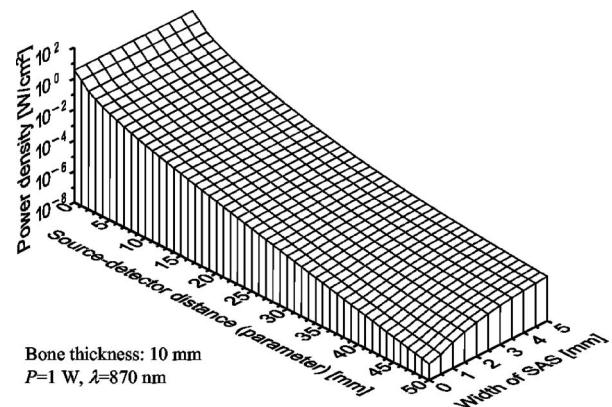
reduce the requirement of the first condition to the contribution of the transmission within anatomical layers deeper than the skin being double that within the skin only, then the source-PD distance should simply exceed 6.5 mm. Summing up, the PD should be positioned at a distance of 6.5 mm to 9.5 mm away from the source.

As to the DD, which receives a signal dependent on the changes of the width of the SAS, its distance from the source should be large enough to guarantee a considerable contribution of radiation propagated within the SAS in relation to the total NIR-BSR received by this detector. Results of our simulations indicate that this contribution will be greater than 10% for source-DD distance exceeding $\approx 16$ mm and greater than 50% for source-DD distance above 36 mm—this position is marked with a vertical line and an arrow in the right part of the Figs. 7 and 8. However, any increase of source-DD distance results in a corresponding decrease of the total power of radiation received by the DD.

### 2.2.2 Results of modeling of NIR propagation within tissues of the head on the side with scalp removed

Simulations of NIR propagation for head model with scalp removed enabled us to verify the contribution of transmission
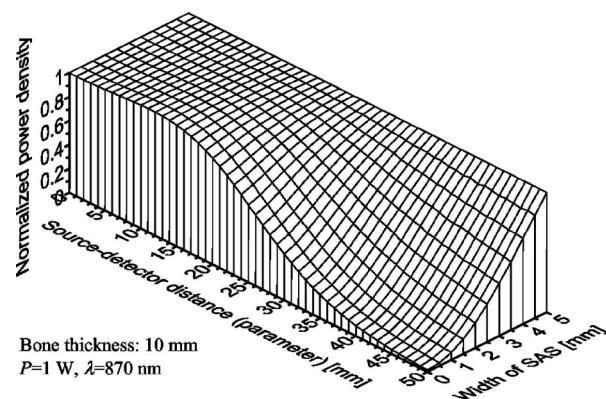


**Fig. 10** Relative changes in received power density of NIR-BSR versus the width of the SAS for a given source-detector distance for the scalp-void part of the head.
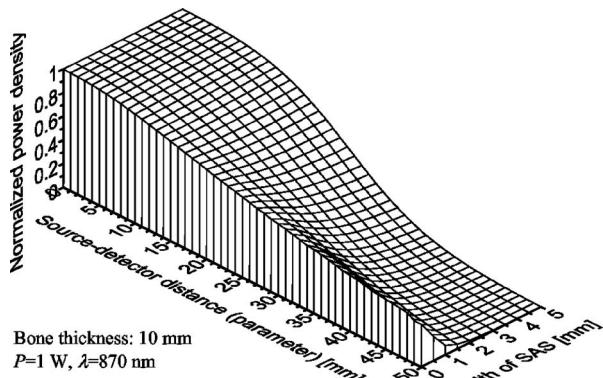
**Fig. 11** Contribution of radiation propagated within the skull bone only to the total NIR-BSR received by the detector as a function of source-detector distance and SAS width for the scalp-void part of the head.



**Fig. 13** Power density of NIR-BSR on the surface of the head and the contribution of radiation: (a) transmitted within the skull bone only, and (b) propagated within the SAS, for SAS width 1 mm and source power of 1 W, for the scalp-void part of the head.

of radiation within particular tissue layers and are particularly valuable for the interpretation of the results of measurements of NIR transmission in the scalp-void part of the head, used to confirm the postulated thesis that—with high source-detector distance—the observed modulation of NIR-BSR intensity is caused mainly by changes in the SAS width, and not by changes in optical parameters of the scalp induced by pulsatile blood flow within the skin. Similar to the case of the head with scalp intact, power densities of NIR-BSR were calculated on the surface of the scalp-void part of the head, and relative changes in received power density versus the width of the SAS for a given source-detector distance for the scalp-void head, and the contributions of powers of radiation transmitted in particular tissue layers to the total power received were measured. Results of modeling are presented in Figs. 9–14.

Comparison of the results of measurements of NIR-BSR intensities on the surface of the head for scalp intact and scalp void in the function of the SAS width reveals their remarkably high similarity. The only significant difference is a few-decibel-higher level of NIR-BSR intensity in the case of the scalp-void part of the head. Considering the earlier suggestions on PD and DD positioning, we should expect the signal received by the PD placed on the scalp to be amplitude-
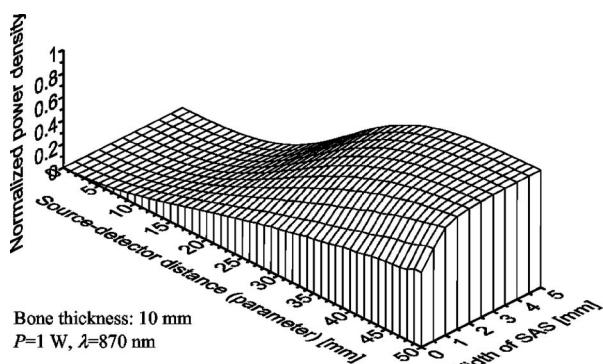
modulated at the heart rate frequency as a result of the changes of optical parameters of the skin, while that should not be the case for the PD placed directly on the skull bone; on the other hand, signals received by the DD should be similar regardless of scalp presence or absence—in both cases, the expected modulation of the signal results from pulsatile changes of the width of the SAS.

## 3 Conclusions

This study shows the influence of changes in the SAS width on the intensity of NIR-BSR with the method of numerical modeling of NIR propagation within anatomical layers of the head in a unique medical case of monolateral traumatic scalp removal. Access to a patient with this rare injury enabled us to collect parameters of particular tissue layers needed for the process of numerical modeling and also to verify the results of measurements of NIR propagation within particular anatomical layers—especially to assess the contribution of transmission within the skin to the total NIR-BSR intensity on the surface of the head. We have demonstrated that the influence exerted on the intensity of that radiation by the changes in the SAS width increases with increasing distance between the source and the detector placed on the surface of the head. Results of this study have also proved that at short source-



**Fig. 12** Contribution of radiation propagated within the SAS to the total NIR-BSR received by the detector as a function of source-detector distance and SAS width for the scalp-void part of the head.
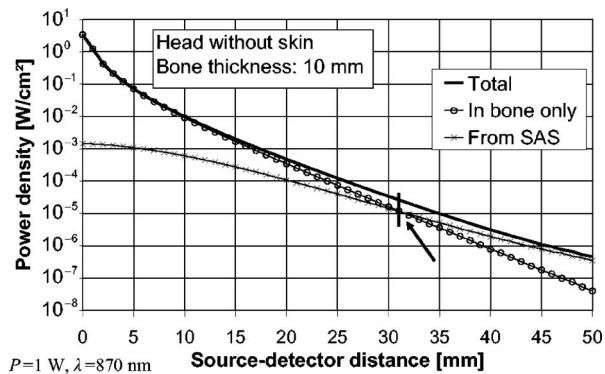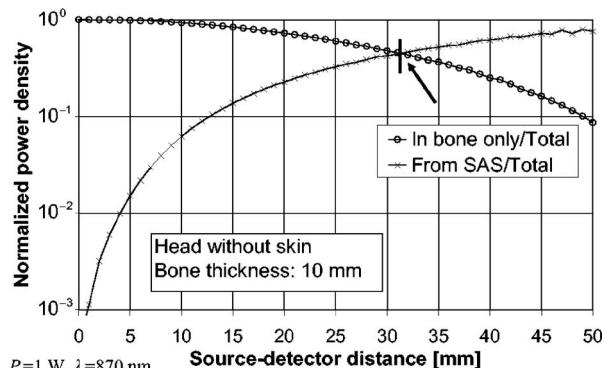


**Fig. 14** Relative contribution of radiation: (a) transmitted in the skull bone only, and (b) propagated within the SAS for the scalp-void part of the head, in the total balance of NIR-BSR.

detector distances, the contribution and influence of NIR transmission within the SAS is negligibly low, which allows for estimation of the influence of the modulation of optical radiation within the scalp on the total intensity of NIR-BSR. The received quantitative results of measurements of intensity of optical radiation in the function of source-detector distance constitute valuable information to be used in the process of designing the source-detector module for the SAS width monitoring with the technique of NIR transillumination. Design of that module and the results of measurements performed with the use of that module are presented in part 2 of this study.[45]

## References

1. J. Wyatt, "Non-invasive brain monitoring with near infrared spectroscopy," *Intensive Critical Care Digest* **8**(3), 47–48 (1989).
2. M. Firbank, M. Schweiger, and D. T. Delpy, "Investigation of light piping through clear regions of scattering," *Proc. SPIE* **2389**, 167–173 (1996).
3. M. Firbank, S. R. Arridge, M. Schweiger, and D. T. Delpy, "An investigation of light transport through scattering bodies with non-scattering regions," *Phys. Med. Biol.* **41**, 767–783 (1996).
4. E. Okada, M. Saito, M. Firbank, and D. T. Delpy, "Monte Carlo investigation of the effect of skull optical properties on optical path length in the brain," *Proc. SPIE* **3194**, 28–33 (1998).
5. E. Okada and D. T. Delpy, "Near-infrared light propagation in an adult head model. I. modeling of low-level scattering in the cerebrospinal fluid layer," *Appl. Opt.* **42**(16), 2906–2914 (2003).
6. E. Okada and D. T. Delpy, "Near-infrared light propagation in an adult head model. II. effect of superficial tissue thickness on the sensitivity of the near-infrared spectroscopy signal," *Appl. Opt.* **42**(16), 2915–2922 (2003).
7. E. Okada, M. Firbank, M. Schweiger, S. R. Arridge, M. Cope, and D. T. Delpy, "Theoretical and experimental investigation of near-infrared light propagation in a model of the adult head," *Appl. Opt.* **36**(1), 21–31 (1997).
8. J. Pluciński, A. F. Frydrychowski, J. Kaczmarek, and W. Juzwa, "Theoretical foundations for noninvasive measurement of variations in the width of the subarachnoid space," *J. Biomed. Opt.* **5**(3), 291–306 (2003).
9. J. Pluciński and A. F. Frydrychowski, "Verification with numeric modelling of optical measurement of changes in the width of the subarachnoid space," *Biocybernetics and Biomedical Engineering* **19**(4), 111–126 (1999).
10. W. N. J. M. Colier, N. J. C. W. van Haaren, M. J. T. van de Ven, H. T. M. Folgering, and B. Oeseburg, "Age dependency of cerebral oxygenation assessed with near infrared spectroscopy," *J. Biomed. Opt.* **2**(2), 162–170 (1997).
11. F. F. Jöbsis, "Non-invasive, infrared monitoring of cerebral and myocardial oxygen sufficiency and circulatory parameters," *Science* **198**, 1264–1267 (1977).
12. J. S. Brazy, D. V. Lewis, M. H. Mitnick, and F. F. Jöbsis van der Vliet, "Noninvasive monitoring of cerebral oxygenation in preterm infants: preliminary observations," *Pediatrics* **75**(1), 217–225 (1985).
13. P. H. Klose, G. D. Lewis, W. P. Messing, R. R. Kasperski, and J. M. Flemming, "Noninvasive infrared cerebral oximetry," *Proc. SPIE* **1641**, 202–207 (1992).
14. P. M. S. O'Brien, P. M. Doyle, and P. Rolfe, "Near infrared spectroscopy in fetal monitoring," *Br. J. Hosp. Med.* **49**, 493–487 (1993).
15. P. Rolfe, Y. A. B. D. Wickramasinghe, and M. Thorniley, "The potential of near infrared spectroscopy for detection of fetal cerebral hypoxia," *Eur. J. Obstet. Gynecol. Reprod. Biol.* **42**, 24–28 (1991).
16. S. Wray, M. Cope, D. T. Delpy, J. S. Wyatt, and E. O. R. Reynolds, "Characterization of the near infrared absorption spectra of cytochrome aa$_3$ and hemoglobin for noninvasive monitoring of cerebral oxygenation," *Biochim. Biophys. Acta* **933**, 184–192 (1988).
17. J. S. Wyatt, M. Cope, and D. T. Delpy, "Quantification of cerebral oxygenation and hemodynamics in sick newborn infants by near infrared spectrophotometry," *Lancet* **2**, 1063–1066 (1986).
18. J. S. Wyatt, M. Cope, and D. T. Delpy, "Responses of cerebral vasculature to changes in arterial carbon dioxide tension measured by near infrared spectroscopy in newborn infants" (abstract), *Pediatr. Res.* **22**, 230 (1988).
19. P. W. McCormick, M. Stewart, M. Dujovny, and J. I. Ausman, "Clinical application of diffuse near infrared transmission spectroscopy to measure cerebral oxygen metabolism," *Hospimedica* **VIII**(4), 39–47 (1990).
20. P. W. McCormick, M. Stewart, M. G. Goetting, M. Dujovny, G. Lewis, and J. I. Ausman, "Noninvasive cerebral optical spectroscopy for monitoring cerebral oxygen delivery and hemodynamics," *Crit. Care Med.* **19**(1), 89–97 (1991).
21. S. A. Weiss, "Biophotonics in action: applying photonic technology to medicine and biology. Spectroscopy reduces brain damage in heart surgery," *Photonics Spectra* **XX**(X), 32–34 (1993).
22. A. F. Frydrychowski, J. Kaczmarek, W. Juzwa, M. Rojewski, J. Pluciński, W. Gumiński, Cz. Kwiatkowski, P. Lass, and T. Bandurski, "Near-infrared-transillumination (NIR-TI)—a new non-invasive tool for exploration of intracranial homeostasis and monitoring of its impairments," *Biocybernetics and Biomedical Engineering* **19**(2), 99–108 (1999).
23. K. Uludag, M. Kohl, J. Steinbrink, H. Obrig, and A. Villringer, "Cross talk in the Lambert–Beer calculation for near-infrared wavelength estimated by Monte Carlo simulation," *J. Biomed. Opt.* **7**, 51–59 (2002).
24. A. H. Hielscher, R. E. Alcuffe, and R. L. Barbour, "Comparison of finite-difference transport and diffusion calculations for photon migration in homogeneous and heterogeneous tissue," *Phys. Med. Biol.* **43**, 1285–1302 (1998).
25. M. Firbank, E. Okada, and D. T. Delpy, "A theoretical study of the signal contribution of regions of the adult head to nearinfrared spectroscopy studies of visual evoked responses," *Neuroimage* **8**, 69–78 (1998).
26. S. R. Arridge, H. Dehghani, M. Schweiger, and E. Okada, "The finite element model for the propagation of light scattering media: a direct method for domain with nonscattering regions," *Med. Phys.* **27**, 252–264 (2000).
27. A. Ishimaru, *Wave Propagation and Scattering in Random Media*, Vol. 1, Academic Press, New York (1978).
28. L.-H. Wang, S. L. Jacques, and L.-Q. Zheng, "MCML—Monte Carlo modeling of photon transport in multi-layered tissues," *Comput. Methods Programs Biomed.* **47**, 131–146 (1995).
29. M. Hiraoka, M. Firbank, M. Essenpreis, M. Cope, S. R. Arridge, P. van der Zee, and D. T. Delphy, "A Monte Carlo investigation of optical pathlength in inhomogeneous tissue and its application to near-infrared spectroscopy," *Phys. Med. Biol.* **38**, 1859–1876 (1993).
30. E. D. Cashwell and C. J. Everett, *Monte Carlo Method for Random Walk Problems*, Pergamon, London (1959).
31. J. H. Curtiss, *Monte Carlo Method*, National Bureau of Standards Applied Mathematics Series 12, Government Printing Office, Washington, DC (1951).
32. W. F. Cheong, S. A. Prahl, and A. J. Welch, "A review of the optical properties of biological tissues," *IEEE J. Quantum Electron.* **26**, 2166–2185 (1990).
33. L. G. Henyey and J. L. Greenstein, "Diffuse radiation in the galaxy," *Astrophys. J.* **93**, 70–83 (1941).
34. R. Marchesini, A. Bertoni, S. Andreola, E. Melloni, and A. E. Sichirollo, "Extinction and absorption coefficients and scattering phase functions of human tissues *in vitro*," *Appl. Opt.* **28**, 2319–2325 (1989).
35. M. S. Patterson, B. C. Wilson, and D. R. Wyman, "The propagation of optical radiation in tissue. 1. models of radiation transport and their application," *Lasers Med. Sci.* **6**, 155–168 (1991).
36. M. S. Patterson, B. C. Wilson, and D. R. Wyman, "The propagation of optical radiation in tissue. 2. optical properties of tissue and resulting fluency distributions," *Lasers Med. Sci.* **6**, 379–390 (1991).
37. J. Pluciński, "Accelerated Monte Carlo method for computation of photon migration by matrix description of photon direction," *Opt. Appl.* **35**(4), 177–983 (2005).
38. C. R. Simpsony, M. Kohl, M. Essenpreis, and M. Cope, "Near-infrared optical properties of *ex vivo* human skin and subcutaneous tissues measured using the Monte Carlo inversion technique," *Phys. Med. Biol.* **43**, 2465–2478 (1998).
39. F. Bevilacqua, D. Piguet, P. Marquet, J. D. Gross, B. J. Tromberg, and C. Depeursinge, "*In vivo* local determination of tissue optical properties: applications to human brain," *Appl. Opt.* **38**(22), 4939–4950 (1999).
40. P. van der Zee, M. Essenpreis, and D. T. Delpy, "Optical properties of

brain tissue," *Proc. SPIE* **1888**, 454–465 (1993).

41. S. L. Jacques, "The role of skin optics in diagnostic and therapeutic uses of lasers," in *Laser in Dermatology*, R. Steiner, Ed., Springer-Verlag, (1990).

42. S. Wan, R. R. Anderson, and J. A. Parrish, "Analytical modelling for the optical properties of the skin with *in vitro* and *in vivo* application," *Photochem. Photobiol.* **34**, 493–499 (1981).

43. S. L. Jacques, *Tissue Optics*, Short Course Notes SC01, SPIE Press, Bellingham, WA (1997).

44. M. Firbank, M. Hiraoka, M. Essenpreis, and D. T. Delpy, "Measurement of the optical properties of the skull in the wavelength range 650–950 nm," *Phys. Med. Biol.* **38**, 503–510 (1993).

45. A. Frydrychowski and J. Pluciński, "New aspects in assessment of changes in width of subarachnoid space with near-infrared transillumination/back-scattering sounding, part 2: clinical verification in the patient," *J. Biomed. Opt.* **12**, 0440XX (2007).

46. C. J. J. Avezaat and J. H. M. Eijndhoven, "Clinical observations on the relationship between cerebrospinal fluid pulse pressure and intracranial pressure," *Acta Neurochir.* **79**(1), 13–29 (1986).

47. C. J. J. Avezaat, J. H. M. Eijndhoven, and D. J. Wyper, "Cerebrospinal fluid pulse pressure and intracranial volume–pressure relationship," *J. Neurol., Neurosurg. Psychiatry* **42**, 687–700 (1979).